2009

UNIVERSITY of CALIFORNIA
Santa Barbara

Testing Quantum Mechanics in a Mechanical System: Characterizing Mechanical Resonators

A dissertation submitted in partial satisfaction of the requirements for the degree of

Bachelor of Science

in

Physics

by

Arnaud Berube

Committee in charge:

Professor Andrew N. Cleland, Chair

June 2009

The dissertation of Arnaud Berube is approved:

Professor Andrew N. Cleland, Chair

May 2009

Testing Quantum Mechanics

in a Mechanical System:

Characterizing Mechanical Resonators

by

Arnaud Berube

I dedicate this thesis, the culmination of my undergraduate career, to my mother and father, who have always stood by my side, supporting me throughout these past four years. I also dedicate this to Zoee, Charles, and Pierrick whom I love very much, my girlfriend Colette who continues to hold my hand through both good times and bad, and all the rest of my friends and family! You have all helped make this possible and I could never have finished this without every one of you. Thank you, for your friendship, for your love, for your support.

Acknowledgements

I would like to thank professor Andrew N. Cleland for taking the time and effort involved in hiring an undergraduate researcher. The experience has been invaluable toward developing my research abilities.

I would also like to express deep gratitude to Aaron O'Connell who has been my graduate mentor throughout my project, providing tremendous support. I am also grateful to professor John Martinis and the Martinis group, who have allowed me to share their lab and have helped in all my technical troubles.

Abstract

Testing Quantum Mechanics

in a Mechanical System:

Characterizing Mechanical Resonators

by

Arnaud Berube

We report on progress towards quantum-limited measurements in mechanical systems; namely, the development of nano-mechanical resonators which will be coupled to quantum bits. The resonators are film bulk acoustic resonators (FBAR's) fabricated in the form of capacitors with a piezoelectric AlN dielectric sandwiched between two Al electrodes, which can be excited electrically into a dilatational resonance mode. The fundamental resonance frequency, determined by the thickness of the Al-AlN-Al structure, is in the 4-7 GHz regime, which matches the required coupling frequency for the qubits. We detail fundamental characterization tests (i.e. lateral geometry, suspension design, coupling capacitors, grounding wire bonds, etc) on the FBARs which display mechanical quality factors of $Q \approx 200 - 300$. We plan to use a superconducting phase quantum bit to perform

quantum limited measurements of the FBARs.

Contents

List of Figures

Chapter 1

Introduction

1.1 Motivation

The limits to the quantum theory are of significant interest to physicists. To date, there has not been a clear experimental test of quantum mechanics in a macroscopic mechanical system. We are developing an experiment to perform such a test. Namely, we are developing an approach in which we plan to transfer quantum states into nano-mechanical resonators from a quantum bit.

1.2 Josephson Phase Qubit

To perform the experiment in consideration, the Josephson phase quantum bit is exploited. This implementation has demonstrated coherence times long enough to perform single and multiple qubit operations [3]. It is, therefore, sufficient to create quantum states for our experiment.

The Josephson phase qubit can be thought of as an inductor-capacitor oscillator, an electrical equivalent to the classical simple harmonic oscillator. Josephson tunnel junctions provide a strong nonlinearity that allows single-photon control over the qubit, which provides a means to create quantum states in the qubit. The qubit is necessarily cooled to temperatures that allow the quantum states to exist without interruption from thermal excitations.

1.3 Coupling to the Qubit

Our implementation of the superconducting phase qubit is optimized for measurements around 6 GHz. Therefore, the approach to couple to the phase qubits involves the development of resonators with a fundamental frequency around 4-7 GHz. The qubits can then be frequency tuned into and back out of resonance with the resonators, allowing the transfer of quantum states into the resonators.

This approach has proven to be quite successful in previous experiments where

qubits were coupled to superconducting electro-magnetic resonators with fundamental frequencies around 6-7 GHz. This technique has provided the ability to generate Fock photon states, measure their decay lifetimes, and even generate arbitrary quantum superpositions of Fock states in the electro-magnetic resonators. Wigner distributions and density matrices of the resulting quantum superpositions were then measured [2].

1.4 The Experiment

In much the same fashion, we plan to couple mechanical resonators to Josephson phase qubits [1]. Our approach for fabricating mechanical resonators in the 4-7 GHz regime involves the exploitation of film bulk acoustic resonators (FBARs) fabricated with piezoelectric aluminum nitride, an idea pioneered by Agilent Technologies. This paper reports on the successful development of such FBARs, detailing fundamental characterization tests of the resonators, which display quality factors of $Q \approx 200 - 300$, sufficient to perform the experiment in consideration.

Chapter 2

FBAR Fabrication

2.1 Piezoelectricity

Piezoelectricity is defined as the ability for certain special materials to generate an electric potential in response to an applied mechanical force. Piezoelectric materials also exhibit the *reverse piezoelectric effect* in which the material produces a mechanical force in response to an applied electric field. Figure 2.1 schematically represents this latter effect. On the left the so called "natural width" of the piezoelectric crystal is displayed. The center shows an expansion in the crystal due to polarization in the structure caused by an applied external electric field. The right displays the reverse polarization caused by an applied external electric field in the opposite direction, causing the crystal to contract.

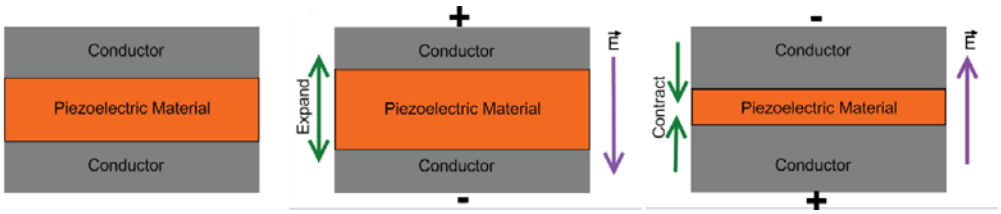

Figure 2.1: Piezoelectric Material – Left: Natural width of crystal. Center: Expansion in crystal due to polarization. Right: Contraction in crystal due to reverse polarization.

2.2 Formulation of the FBAR

The general design in the formulation of film bulk acoustic resonators is to exploit a piezoelectric crystal as a dielectric in a *Conductor-Piezoelectric Crystal-Conductor* parallel plate capacitor. Figure 2.2 displays a schematic of such a parallel plate capacitor, with aluminum conductors and aluminum nitride piezoelectric crystal.

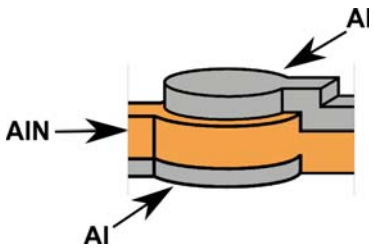

Figure 2.2: FBAR Parallel Plate Capacitor – Al-AlN-Al parallel plate capacitor with AlN acting as the piezolectric dielectric.

This parallel plate capacitor has an electrical capacitance C_0 given by the usual

equation for a parallel plate capacitor with a dielectric:

$$C_0 = \frac{\epsilon_0 \epsilon_{AlN} A}{d} \tag{2.1}$$

where ϵ_0 is the permittivity of free space, $\epsilon_{AlN} \approx 8.9$ is the permittivity of AlN, A is the lateral area of the capacitor plates, and d is the vertical distance between the two plates.

The capacitor also has a mechanical response due to the piezoelectric response of the AlN dielectric that, combined with the electrical capacitance, can effectively be modeled by the circuit of Figure 2.3.

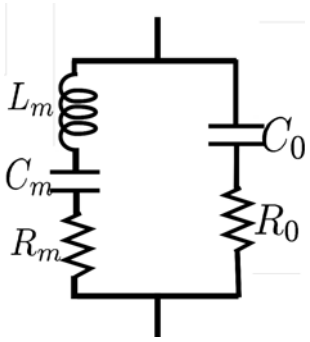

Figure 2.3: FBAR Equivalent Electrical Circuit – Circuit modelling both electrical and mechanical response of the parallel plate capacitor.

where L_m and C_m electrically model the inertial and spring response of the mechanical resonator, C_0 is again the electrical capacitance, and R_m and R_0 represent the mechanical and electrical loss.

Such a model has two resonances associated with it: a series resonance between L_m and C_m that acts as a short (not a perfect short because of loss due to the resistance R_m) between the two terminals, and a parallel resonance between L_m, C_m, and C_0 that acts as an open (not a perfect open because of the loss due to combined resistance $R_m + R_0$) between the two terminals. The latter of these two is our resonance of interest because it allows for the storage of quantum states.

The fundamental dilatational mode of this resonance is the mode of interest for our experiment because it is the easiest mode to couple to. The frequency of this mode of the FBAR is given by:

$$f = \frac{v_{sound}}{2d}, \tag{2.2}$$

where V_{sound} is the average sound velocity for both Al and AlN and d is the total thickness of the capacitor. With this frequency equation, we can relatively easily tune the resonance frequency to the correct 4-7 GHz frequency by simply varying d.

2.3 The Fabrication Process

Film bulk acoustic resonators are currently used commercially as mechanically-based filters of electronic signals, developed for the 1.8 GHz mobile telephone

frequency band. These commercially available FBARs achieve quality factors in excess of a few thousand at this frequency, making the technology appealing for quantum measurements. Unfortunately, our phase qubit is optimized for measurements around 6 GHz. Also, excessive stray capacitance and inductance from coupling requires that the resonator be in close proximity to the qubit. We have therefore developed a new resonator fabrication process based on the commercial process but modified for our applications.

Figure 2.4 displays the seven major steps in our fabrication sequence. We start with an unprocessed silicon wafer and then deposit our first layer of aluminum to about 130 nm. This layer is then etched to form the resonator base electrode. Next, we deposit the aluminum nitride dielectric to the appropriate thickness for the resonance frequency we are fabricating for. After this, we etch a via down to the base aluminum layer and deposit another 130 nm layer of aluminum. We then etch this top layer to form the top electrode. Finally, we etch the excess aluminum nitride to form the desired parallel plate capacitor and then suspend the capacitor with an isotropic xenon diflouride etch of the underlying Si.

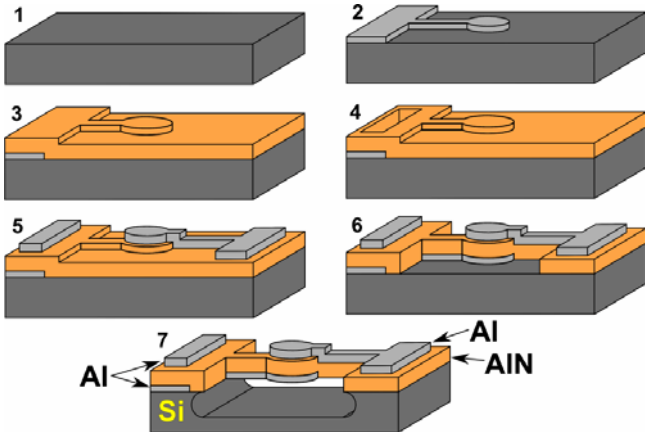

Figure 2.4: FBAR Fabrication Sequence – 1.Unprocessed wafer. 2.Deposit and etch Al. 3.Deposit AlN. 4.Etch via. 5.Deposit and etch Al. 6.Etch excess AlN. 7.Suspend using isotropic XeF_2.

2.4 Building XeF_2 Etching Equipment

The final step of our fabrication sequence proved to require additional equipment. To allow the fundamental dilatational mode to oscillate effectively with minimal loss, we needed to suspend the capacitor. This required an isotropic thin film etch of the silicon base, a process not immediately available to us in our clean room. We therefore decided to build such an instrument, exploiting xenon diflouride, a gaseous compound that attacks the silicon base and turns it into a new gaseous compound, isotropically etching the silicon, as desired.

We modeled our equipment after an established design from NIST. Figure 2.5 displays a photograph of our finalized XeF_2 etcher. The red outline in Figure 2.5

displays the vital components, which we ordered and assembled (ethcing chamber and mixing chamber). Then, as pointed out with the yellow arrows of Figure 2.5, the various pneumatic valves controlling the flow of gases were attached via stainless steel piping. In the blue circles of Figure 2.5, the input and output gas lines are displayed. Because xenon diflouride is a toxic gas, we had to be careful about properly handling the input and output gases. Next, the green outline of Figure 2.5 presents the electrically controlled solenoid valves that were used to control the pneumatic valves. Finally, the orange outline of Figure 2.5 shows the relay board and the small analog to digital converter used in the computer interfacing, and the purple box displays the power sources used to power the electronics and the fan.

We built the instrument in commercially available framing from 80/20 Inc., with some added custom support systems. Then we enclosed the equipment with aluminum panels machined in our machine shop. To complete the xenon diflouride etcher, we created a computer program to control operation. Before we could run the instrument, however, we had to perform various leak tests to ensure that the system was under vacuum. After fixing the leaks and debugging the software, we were able to start suspending our devices. With our finished fill-and-purge low vacuum XeF_2 system we achieve etch rates of 4 μm/min with a sublimation pressure of $\sim$ 3 torr. We dilute the vapor with helium gas. Figure 2.6 displays

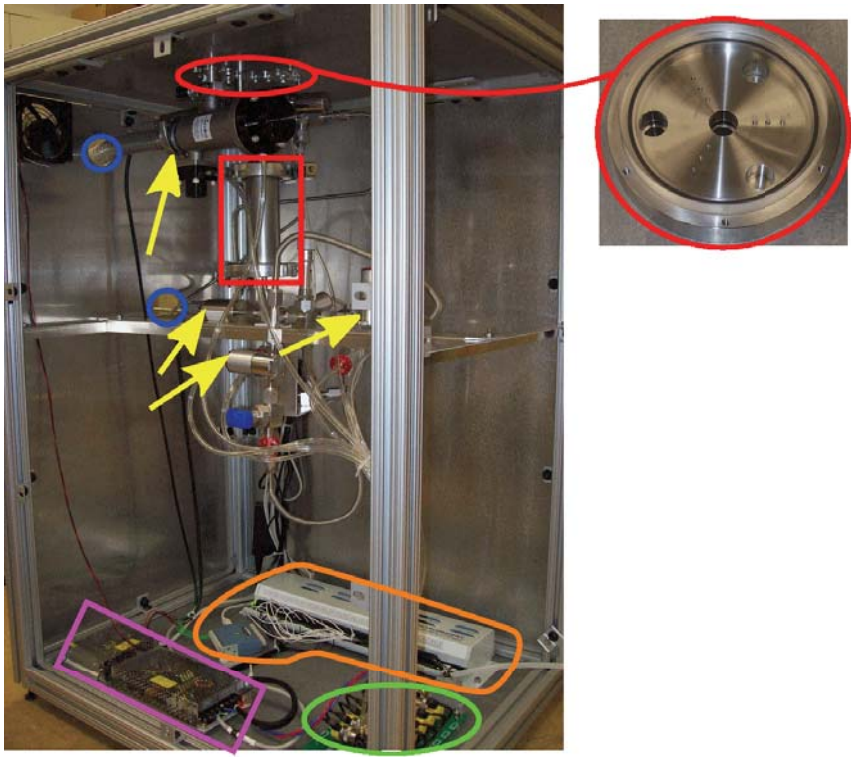

Figure 2.5: XeF_2 Etcher – Red) Etching chamber (top and bottom view) and mixing chamber. Yellow) Pneumatic valves. Blue) Input/output gas lines. Green) Solenoid valves. Orange) Relay board and A/D converter. Purple) Power sources.

two of our first released FBARs.

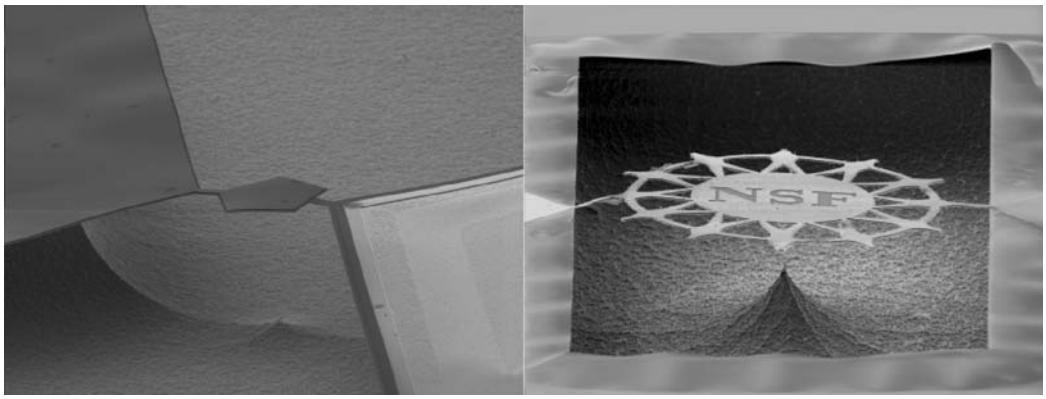

Figure 2.6: SEM of Etched FBARs – Left: One of the first suspended capacitors. Right: A neat release for our funding source.

This effectively concluded the fabrication of our film bulk acoustic resonators.

Chapter 3

Measuring the FBARs

3.1 Microwave Mounts

To measure the film bulk acoustic resonators we mount the die containing the resonator on a two-port microwave mount. We use two different mounts, a copper mount and an aluminum mount, displayed in Figure 3.1. The blue box surrounding the dies represents the mount's electrical ground and the red bars represent bond pads used to measure signal between the two SMA ports.

On the die itself, we place the FBARs directly between two on-chip interdigitated coupling capacitors, as can be seen in Figure 3.2. The equivalent circuit diagram is also displayed in Figure 3.2 (remember, the RLC circuit in the middle is the FBAR equivalent circuit). This acts as our measurement circuit. The top

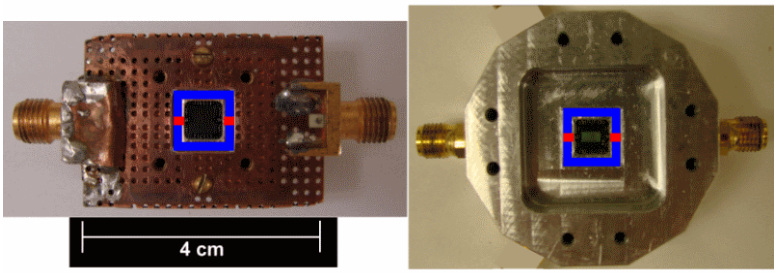

Figure 3.1: Microwave Mounts – Left: Copper mount. Right: Aluminum mount. Blue boxes: Electrical ground of mounts. Red bars: Measuring bond pads.

electrode of the capacitor is connected to the die's ground plane, which is then connected to the mount's electrical ground via many 25 μm diameter aluminum wire bonds. The base electrode is connected to the on-chip interdigitated coupling capacitors (Cc), which are then followed by two 50 Ω coplanar waveguides, which terminate in wire-bond pads. We then wire bond from these bond pads to the mount's transmission bond pads. In this way, we can measure the transmission through the mount and calculate the device impedance $Z(\omega)$.

3.2 Microwave Measurements

To measure the transmission through the mount, we use an Agilent PNA series microwave vector network analyzer, pictured in Figure 3.3. This instrument is a microwave source that sweeps frequencies from 20 MHz to 20 GHz out Port 1 and

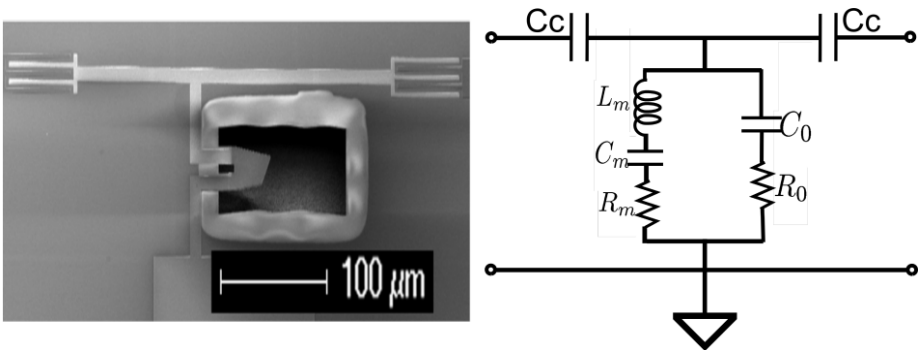

Figure 3.2: Measurement Circuit – Left: SEM of measurement circuit. The center quadrillateral is the FBAR. The top corners display the coupling capacitors. Right: Equivalent circuit. The center RLC circuit represents the FBAR.

then measures the transmission coefficient $S_{21} = 2V_1/V_2$ at Port 2.

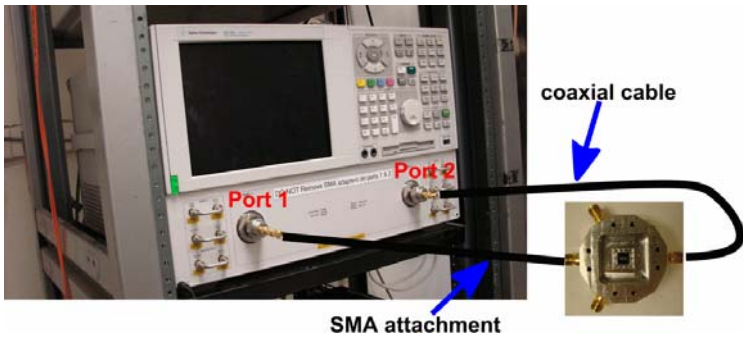

Figure 3.3: PNA to Mount – Vector network analyzer attached to mount.

As can be seen in Figure 3.3, we attach the mount directly to Port 1 with an SMA attachment, and then we connect Port 2 to the other side of the mount via a short coaxial cable.

At this point, we are able to make measurements of our resonators. Figure 3.4

shows a typical measurement of $|S_{21}|$ as a function of frequency. Our next task, then, is to understand what our data means.

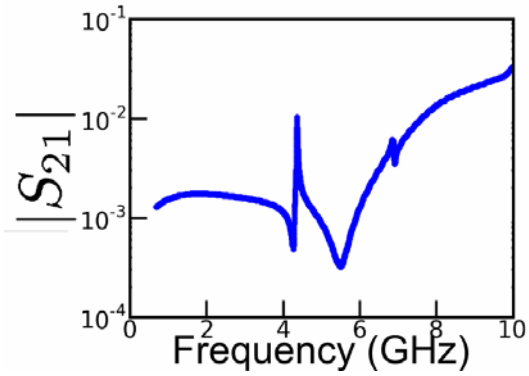

Figure 3.4: Generic Plot of Transmission – Plot of $|S_{21}|$ as a function of frequency.

Chapter 4

Analyzing Techniques

4.1 The Equivalent Resonator Circuit

As mentioned in Chapter 2, the mechanical resonator presents us with two resonances. Figure 4.1 reproduces the equivalent circuit model of our resonator with the frequency response data.

The lowest frequency resonance in the data, the local minimum around 4 GHz, is believed to be a series resonance caused by L_m and C_m, the mechanical inductance and capacitance. A series resonance creates a short across its circuit elements at the resonance frequency, causing the transmission through our measurement circuit to drop to its minimum, hence displaying a local minimum in the data. The frequency for this resonance is given by:

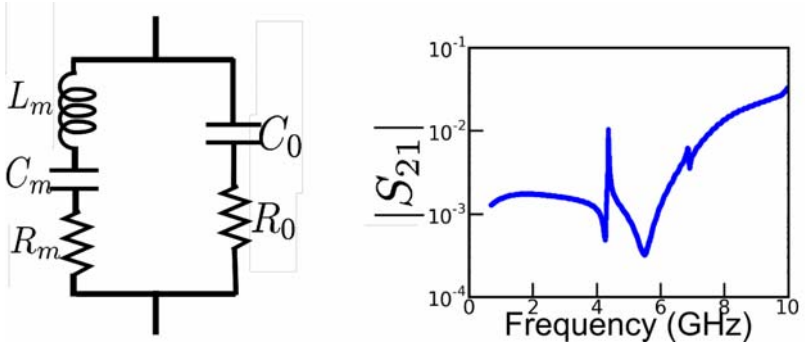

Figure 4.1: Equivalent Resonator Circuit and Frequency Response – Left: The electrical circuit equivalent of our mechanical resonator. Right: The transmission $|S_{21}|$ as a function of frequency (reproduced from Figure 3.4).

$$\omega_m = \frac{1}{\sqrt{L_m C_m}} \tag{4.1}$$

The next higher frequency resonance in the data, the local maximum immediately after the series resonance dip, is a parallel resonance caused by L_m and $C_m \| C_0$, the mechanical inductance and effective mechanical/electrical capacitance. A parallel resonance creates an open across its circuit elements at the resonance frequency, causing the transmission through our measurement circuit to peak to its maximum, hence displaying a local maximum in the data. The frequency for this resonance is given by:

$$\begin{aligned}
\omega_0 &= \frac{1}{\sqrt{L_m C_{eff}}} \\
&= \frac{1}{\sqrt{L_m (C_m \| C_0)}} \\
&= \frac{1}{\sqrt{L_m C_m (1 + C_0/C_m)}} \\
&= \omega_m \sqrt{1 + \frac{C_m}{C_0}}. \qquad (4.2)
\end{aligned}$$

From the two resonances we can extract L_m and C_m; C_0 is given by the geometry and dielectric response of the AlN.

4.2 Modelling the PNA Measurement

We also need a model for the PNA vector network analyzer circuit. To do this, we can replace our model measuring circuit of Figure 3.2 (right), which models only the circuit elements on the die (namely, the resonator and the coupling capacitors), with the model shown in Figure 4.2.

L_m, C_m, and R_m model the mechanical properties of the resonator. C_0 and R_0 represent the electrical capacitance and loss of the resonator. Cc is the capacitance of the coupling capacitors. R refers to the 50 Ω impedance due to the transmission line and interior PNA impedances. V_1 is the output voltage from the PNA and V_2 is the measured voltage at Port 2.

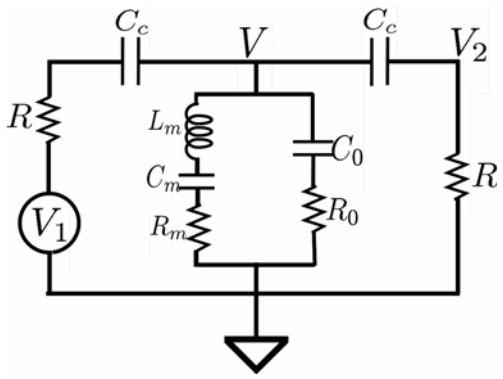

Figure 4.2: Equivalent Measurement Circuit with PNA – The electrical circuit corresponding to: PNA output voltage (V_1), transmission through the mount, and PNA transmitted voltage (V_2) as measured at Port 2

With this circuit, we can model $|S_{21}|$ as a function of frequency. The first step is to find the Norton equivalent model of the circuit (pictured in Figure 4.3), where Z_C is the impedance of the coupling capacitors ($Z_C = 1/\imath\omega Cc$).

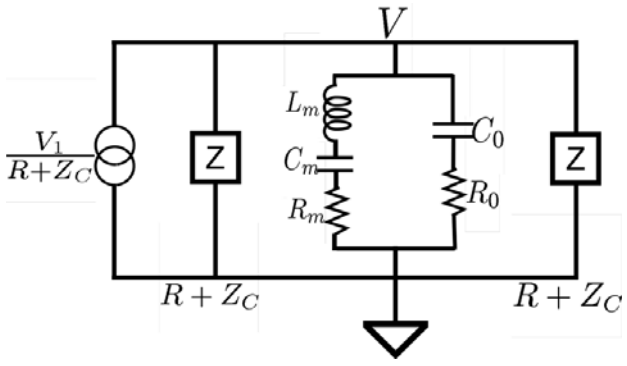

Figure 4.3: Norton Equivalent of PNA Measurement Circuit – The Norton equivalent of Figure 4.2.

From this circuit, it is relatively straight forward to calculate V:

$$\begin{aligned} V &= I_{eq} Z_{eff} \\ &= \left[\frac{V_1}{R+Z_C}\right] * \left[(R+Z_C) \| (R+Z_C) \| Z_{res}\right]. \end{aligned} \tag{4.3}$$

And then, use the voltage divider formula to get V_2:

$$V_2 = V \frac{R}{R+Z_C}. \tag{4.4}$$

Finally, we know $S_{21} = 2V_2/V_1$ so that, combining equations 4.3 and 4.4:

$$\begin{aligned} S_{21} = 2\frac{V_2}{V_1} &= 2\left[\frac{R}{R+Z_C}\right] * \left[\left(\frac{1}{R+Z_C}\right) * \left(\frac{1}{2}(R+Z_C) \| Z_{res}\right)\right] \\ &= \left[\frac{R}{(R+Z_C)^2}\right] * \left[(R+Z_C) \| Z_{res}\right] \\ &= \frac{R}{(R+Z_C)^2} \frac{(R+Z_C) Z_{res}}{(R+Z_C)+Z_{res}} \\ &= \frac{R}{R+Z_C} \frac{Z_{res}}{R+Z_C+Z_{res}}. \end{aligned} \tag{4.5}$$

We then use the modulus of this equation, fitting parameters for the various elements that make up Z_{res} (namely L_m, C_m, R_m, and R_0), and generate a simulated plot of our data. Figure 4.4 displays a plot of the simulation of the data shown in Figure 3.4. Though we could not yet fit the dip around 5.5 GHz (this dip will be discussed in Chapter 5), we were able to make a reasonable fit of our data with this model circuit.

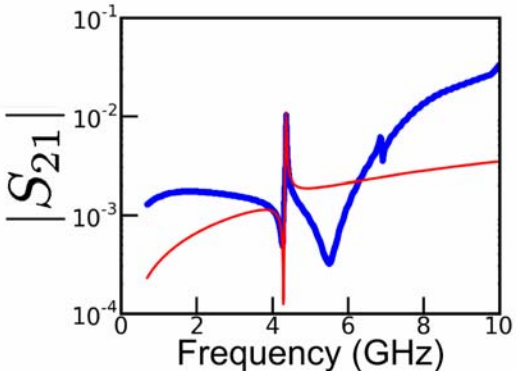

Figure 4.4: Generic Fit of Transmission – Red: Fit of $|S_{21}|$ as a function of frequency. Blue: Measured $|S_{21}|$ as a function of frequency.

4.3 The Quality Factor

Another parameter of an RLC circuit is the quality factor (Q). Q is a dimensionless quantity that is defined as the energy stored divided by the energy dissipated per cycle. The very general formula for Q is given by:

$$\begin{aligned} Q &= 2\pi \left(\frac{energy\,stored}{energy\,dissipated\,per\,cycle} \right) \\ &= \omega \left(\frac{energy\,stored}{power\,lost} \right). \end{aligned} \tag{4.6}$$

Q therefore gives a measure of the "quality" of a resonator, describing for how many cycles the energy will be stored in the resonator at its resonance frequency. Q for a parallel RLC resonator is given by:

$$\begin{aligned} Q &= \frac{1}{R}\sqrt{\frac{L}{C}} \\ &= \frac{\omega_0 L}{R}, \end{aligned} \tag{4.7}$$

where, for our resonator, $R = R_m + R_0$, $L = L_m$, and ω_0 is defined by equation 4.2.

4.4 Quantifying Results: The Energy Decay Time

The quality factor alone is simply a dimensionless quantity describing the energy stored per energy lost per cycle. A more useful parameter for quantum limited experiments is the energy relaxation time (T_1). Physically, T_1 describes approximately the time over which a single phonon will remain in the resonator before decaying. The equation for T_1 is:

$$T_1 = \frac{Q}{\omega_0}. \tag{4.8}$$

From previous experiments with electro-magnetic resonators, we know that it is possible to couple a quantum bit to a resonator and make meaningful measurements of quantum states with a minimum $T_1 \approx 2$ ns. Also, because the qubit's optimal operation frequency is around 6 GHz, we want our resonators operating

with a resonance frequency of about the same value. This means that we need to make resonators whose resonance frequency will be a couple GHz higher than the resonance frequency of Figure 3.4. With such resonators, we need $Q \gtrsim 100$. The quality factor of Figure 4.4 is $Q \approx 200$, but not resonating at the appropriate frequency. This data, however, gave us hope of achieving our final goal.

Chapter 5

Data and Results

This chapter outlines various tests we performed in an attempt to understand and characterize our film bulk acoustic resonators.

5.1 The Unknown Dip

Our first concern with our theoretical fit was that it did not model the dip we were consistently measuring after our mechanical resonances, appearing at about 5.5 GHz in Figure 4.4. Our theory was that there was an additional resonance being introduced due to some added inductive element which our model circuit did not take into account. We believed that this inductance was a line-inductance caused by the leads connecting the FBAR's electrodes to the measurement circuit

and to ground (the highlighted leads of the measurement circuit pictured in Figure 5.1 (left)). Figure 5.1 (right) shows how this added inductive element would look in our model.

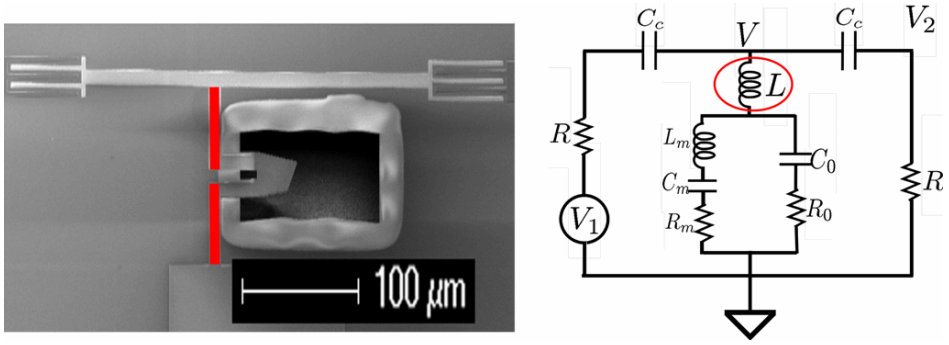

Figure 5.1: Line Inductance and Equivalent Circuit – Left: Reproduced SEM of a quadrillateral FBAR and the on-chip measurement circuit, highlighting the leads in question. Right: Equivalent circuit with this new inductance element added.

The test we performed to confirm our theory was simply to vary the on-chip lead length of our measurement dies. In addition, we changed the dielectric of our capacitor to a non-piezoelectric material so that we could eliminate the mechanical resonances in order to better understand the origin of the unwanted resonance, and to ensure that the resonances we observe are indeed mechanical ones.

The inductance caused by a wire is proportional to the wire length. By varying the inductance we expected to effectively alter the resonance frequency (remember, $\omega_{LC} = 1/\sqrt{L_{line}C_{eff}}$). Our data from this test is displayed in Figure 5.2.

Notice that as we increased the lead length, we effectively *lowered* the dip

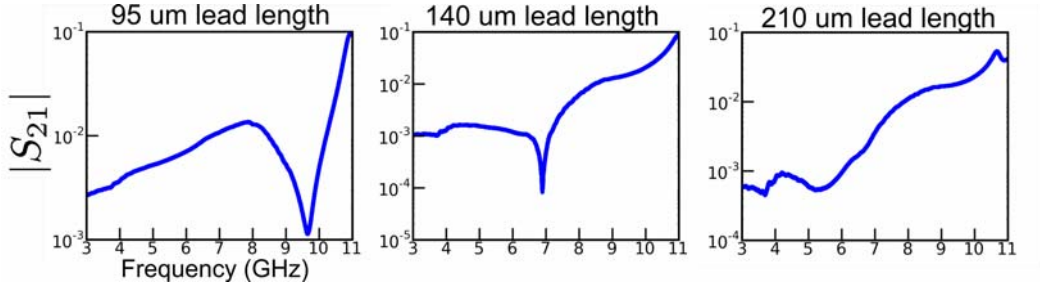

Figure 5.2: Data: Line Inductance Test – Three circuits with varying lead lengths, using an electrical capacitor (no piezoelectric dielectric).

frequency, as predicted. We therefore added an inductor to our theoretical circuit, as shown in Figure 5.3 (left). With this new circuit, we were able to model the dip accurately, as can be seen in the new fit of Figure 5.3 (right). With this new fit, we still see the same quality factor as our previous fit, namely $Q \approx 200$, but the new fit provides a more reassuring match to the data.

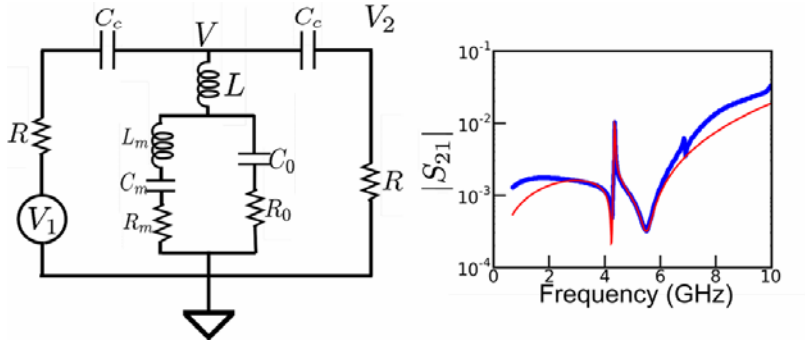

Figure 5.3: Modifying the Theoretical Circuit – Left: Adding an inductor to our theoretical circuit. Right: Plot of a fit of $|S_{21}|$ with the modified circuit.

5.2 Test: Mechanical Resonance

One of our most important preliminary tests was to understand whether we were measuring mechanical resonances or some other physical anomaly. We performed two tests to measure this.

5.2.1 Step Release

The first test involved simply taking one of our resonators and releasing it in the XeF_2 etcher in steps, measuring the resonator at each step. Figure 5.4 shows the data from these measurements.

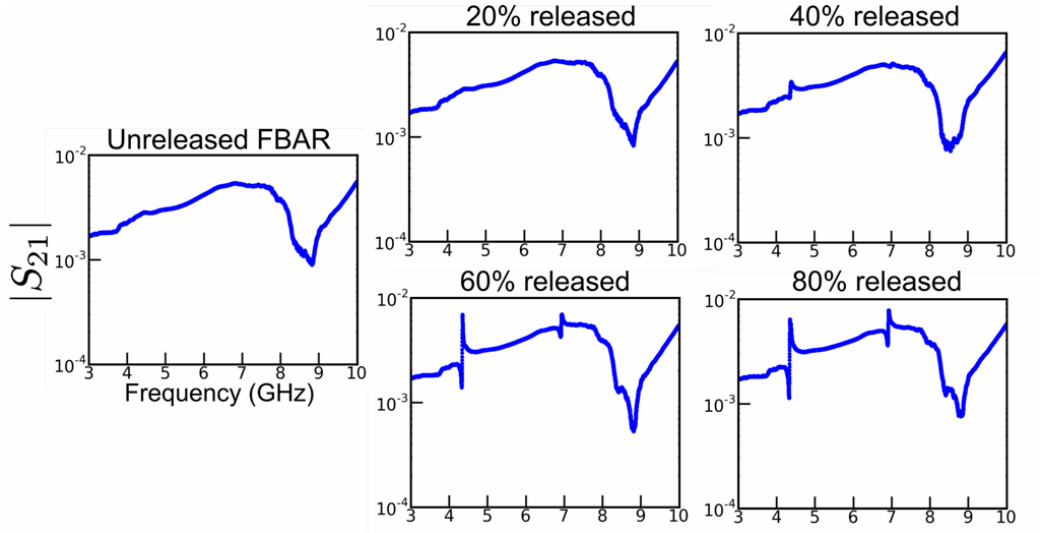

Figure 5.4: Step Release Data – Plots of a resonator released in 20% intervals.

As expected of a mechanical resonance, the resonant modes are not visible until the capacitor is about 40% suspended, and then become more pronounced at 60% and 80% release.

One feature that we still do not understand that is very pronounced in this data is the other resonances appearing at around 7 GHz. They seem to be mechanical, but they do not match the calculated frequency of the next resonance mode ($freq = 3v_{sound}/2d$). These higher frequency modes, however, do not effect our modes of interest, so we simply chose to ignore them.

5.2.2 Mechanical versus Electrical Dielectric

We performed one other test to check that we were indeed measuring mechanical resonators. This test involved the fabrication of two identical structures, one with a mechanical (piezoelectric) AlN dielectric and the other with a non-piezoelectric SiN dielectric. Figure 5.5 shows the data from these two capacitor measurements.

Notice that the SiN dielectric does not display resonant modes at the resonance frequency (∼4.5 GHz) for a piezoelectric resonator. The AlN piezoelectric dielectric, on the other hand, does display the expected resonances. We therefore do have *mechanical* resonators.

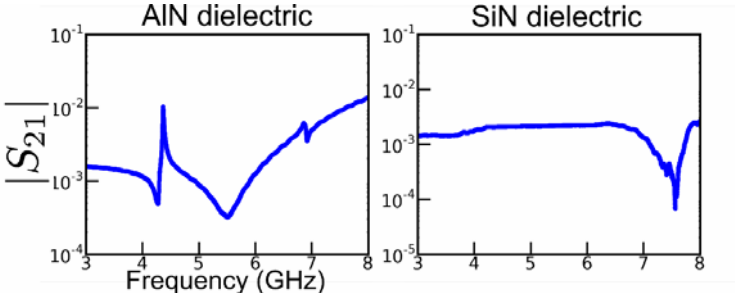

Figure 5.5: Dielectric Data – Plots of a capacitor with two different dielectrics.

5.3 Test: Grounding Bonds

Wire bonding the FBARs to the mounts turned out to be rather difficult, so we wanted to test whether more wire bonds made a visible difference in our data. The theory was that many wire bonds were necessary to reduce the inductance from each connection as well as to reduce coupling to stray electromagnetic resonance modes in the mounts. As displayed in the plots of Figure 5.6, the theory unfortunately turned out to be accurate. We measured more electrically isolated data if we used maximal wire ground bonds, so we ensured from this point onward in our measurements to continue using maximal wire bonds.

This data was discomforting because the resonances did not look like our predicted mechanical resonance modes (a dip followed by a peak). We were therefore led to make two more tests: the first to discover why we only measured the me-

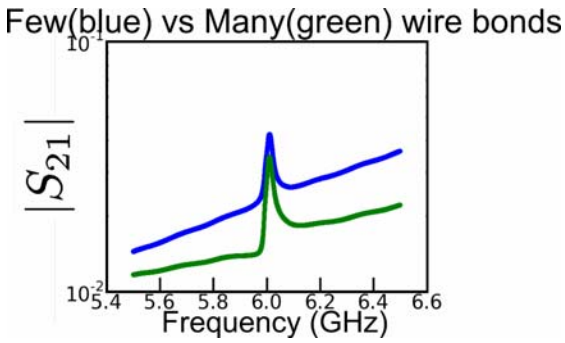

Figure 5.6: Ground Bond Data – Plots of the same resonator measured with different numbers of electrical ground wire bonds.

chanical resonance peaks in Figure 5.6 and not the dips; and the second to ensure that two identical resonators produced the same measurement data (to show that this grounding bond data was not simply due to the error bar produced by measuring two different devices).

5.4 Test: Mount

From the beginning, we had the option of using either of the two microwave mounts of Figure 3.1. We thought that we might measure more consistent and electrically isolated data in one of the mounts, so we compared measurements with the two different mounts. Figure 5.7 displays measurements of two different resonators (same growth conditions) taken from the two mounts.

The copper mount is so electrically disruptive that the mechanical dip reso-

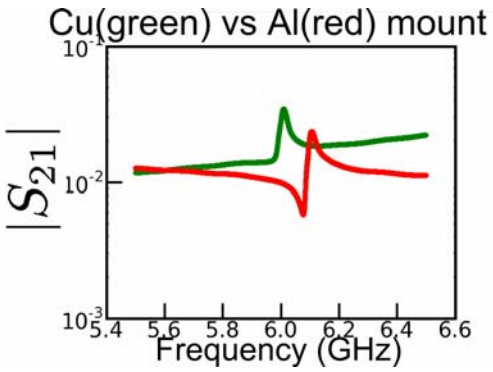

Figure 5.7: Data from the two Mounts – Plots of two resonators under the same growth conditions measured in different mounts.

nance is not even visible in the data. The aluminum mount, on the other hand, clearly displays the features of interest in the data. From this point onwards we only used the aluminum mount for our data taking.

Also, we realized from this test that the lack of measurement of the dip resonance from the wire bond test (see Figure 5.6) was caused by measuring the FBARs in the copper mount. After changing solely to the aluminum mount, we never saw this lack of dip again.

5.5 Test: Reproducable Data

The mount test answered one of the questions posed from the grounding bond test. We then tested the reproducibility of the measurement between two identical resonators to answer the second question. The data from these tests are displayed

in Figure 5.8.

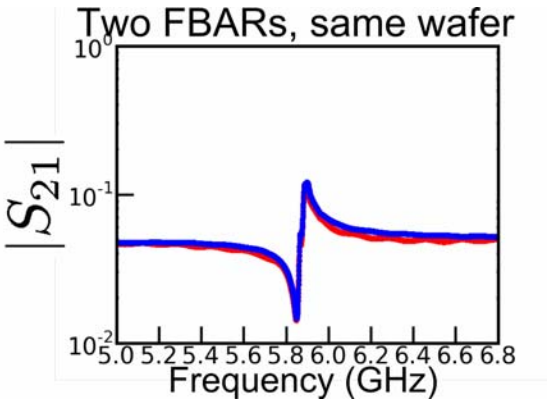

Figure 5.8: Reproducability – Plots of two identical resonators.

As can be seen, we were able to reproduce our results. This effectively answered the question at hand.

5.6 Test: Coupling Capacitors

The last part of our circuit that we did not yet have a good grasp of was the coupling capacitors. There were two concerns: was our resonance quality factor being limited by having coupling capacitors that were too large, or were we losing some of our signal by having coupling capacitors that were too small. We therefore decided to see if we could optimize the coupling capacitors (see Figure 3.2 for a reminder of what the coupling capacitors are). We measured identical

FBARs with two different coupling capacitors, 10 fF and 50 fF. The measurement data and the fits can be seen in Figure 5.9. Notice that, because the coupling capacitors define how much signal is transmitted, the 50 fF Ccs have a much higher transmission than the 10 fF Ccs.

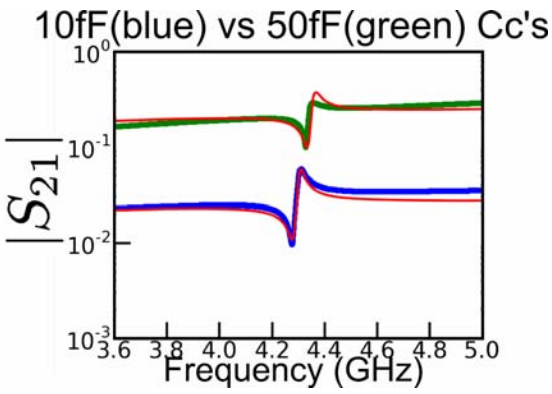

Figure 5.9: Coupling Capacitor Test – Plots of two identical resonators measured with different coupling capacitors. The fits are also plotted.

The quality factors for the fits are: $Q_{10fF} = 165$ and $Q_{50fF} = 185$. Notice, however, that we could not fit the data to great accuracy; to the extent that the error bar in the fit is greater than the mere 20 difference in Q. We therefore could not conclude any differences in the coupling capacitors from this test.

Next, we performed a calculation to see if the measured Q was being limited by having big coupling capacitors. This calculation involved quantifying the quality factor of our measurement circuit in the absence of loss from the resonator (the only loss elements then are the 50 Ω impedances due to the transmission lines

and interior impedances of the PNA (labeled R)). The circuit then looks like Figure 5.10 (left) in which the complex impedance elements $Z = R + Z_C$ can be transformed (to great approximation) into a parallel resistor and capacitor combination with $Resistance = |Z_C|^2/R$ and $Capacitance = Cc$. This transformed circuit is displayed in Figure 5.10 (right).

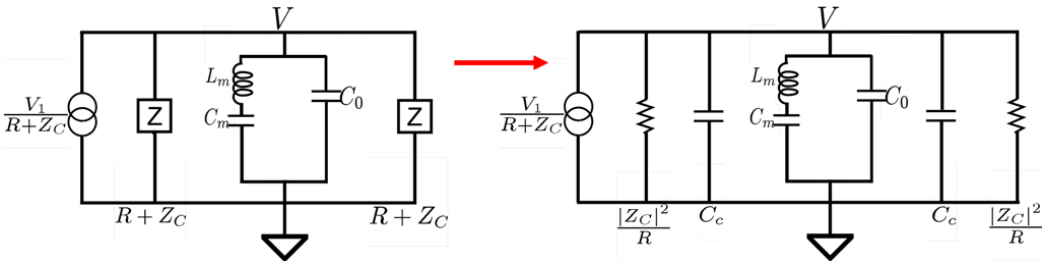

Figure 5.10: Limiting Quality Factor Circuit – Circuit sketch of an ideal FBAR being limited by the quality factor of the measurement circuit.

The quality factor of this circuit is described by the inverse of the results of equation 4.7:

$$
\begin{aligned}
Q_{lim} &= \frac{R_{eff}}{\omega_0 L_m} \\
&= \frac{\left(\frac{|Z_C|^2}{R} \| \frac{|Z_C|^2}{R}\right)}{\omega_0 L_m} \\
&= \frac{|Z_C|^2}{(\omega_0 L_m)(2R)} \\
&= \frac{\left(\frac{1}{\omega_0 Cc}\right)^2}{(\omega_0 L_m)(2R)} \\
&= \frac{1}{2\omega_0^3 R L_m Cc^2}.
\end{aligned} \tag{5.1}
$$

The calculated limiting quality factors for the range of fitting parameters we use for L_m and Cc range from 20000 to 80000 for the 10 fF coupling capacitors and from 800 to 3000 for the 50 fF coupling capacitors. This calculation effectively displayed that the 50 fF coupling capacitors were not limiting the resonance quality factors we were measuring.

We therefore found no difference between using 10 fF versus 50 fF coupling capacitors. The Q_{lim} parameter for the 50 fF coupling capacitors, however, was bordering on the Q that we hoped to see in our FBARs, so we decided to solely use 10 fF coupling capacitors from this point onwards.

5.7 Test: FBAR Legwidth

At this point in our testing of the film bulk acoustic resonators, we understood the major features of our data and our measuring instruments. We therefore decided to start optimizing our FBARs by testing design parameters.

The first design parameter to test was the width of the legs that attach the suspended FBARs to the chip (see Figure 5.11).

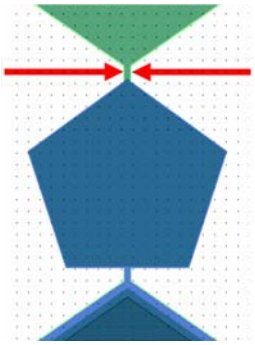

Figure 5.11: Legwidth Schematic – A schematic of an FBAR, pointing out the legwidth between the two red arrows, which supports the suspended device.

It was reasonable to assume that there was mechanical loss due to this feature, so we wanted to make the legwidth as small as possible. At the same time, there was a trade-off in that the high stress caused by suspending our FBARs often caused smaller legwidth designs to break. We therefore tested two identical capacitors with different legwidths. The data from these tests are displayed in Figure 5.12.

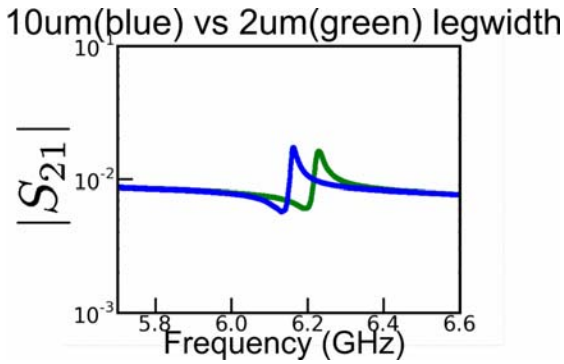

Figure 5.12: Legwidth Test – Plot displaying the measurements from two identical capacitors with different legwidths.

Notice that the resonator with a bigger legwidth has lower frequency resonance modes. Apparently the legwidth slightly changes the electrical capacitance, which affects the resonance frequencies (see equations 4.1 and 4.2).

The quality factor for these measurements was calculated (via equation 4.7) to be 205 for the 2 μm legwidth FBAR and 240 for the 10 μm legwidth FBAR. This slight difference suggests that a larger legwidth leads to a higher Q, but the difference actually is not enough to conclude anything. The test simply displays that the legwidth does not seem to affect Q.

5.8 Test: FBAR Geometry

The other design parameter to test was the geometry of the FBAR capacitor. We tested squares, pentagons, and quadrillaterals with no parallel sides. We also

varied the electrical capacitance of the FBARs (by varying the area of the capacitor) from 0.025 pF to 0.54 pF. The data measured from these various geometries are displayed in Figure 5.13, along with schematics of their geometries, fits of the data, and the quality factors calculated from the fits.

From this data, we were not able to conclude anything. It seems that there is no correlation between geometry and Q or between the electrical capacitance and Q. There is something else limiting our measured Q to about 250 that we do not understand.

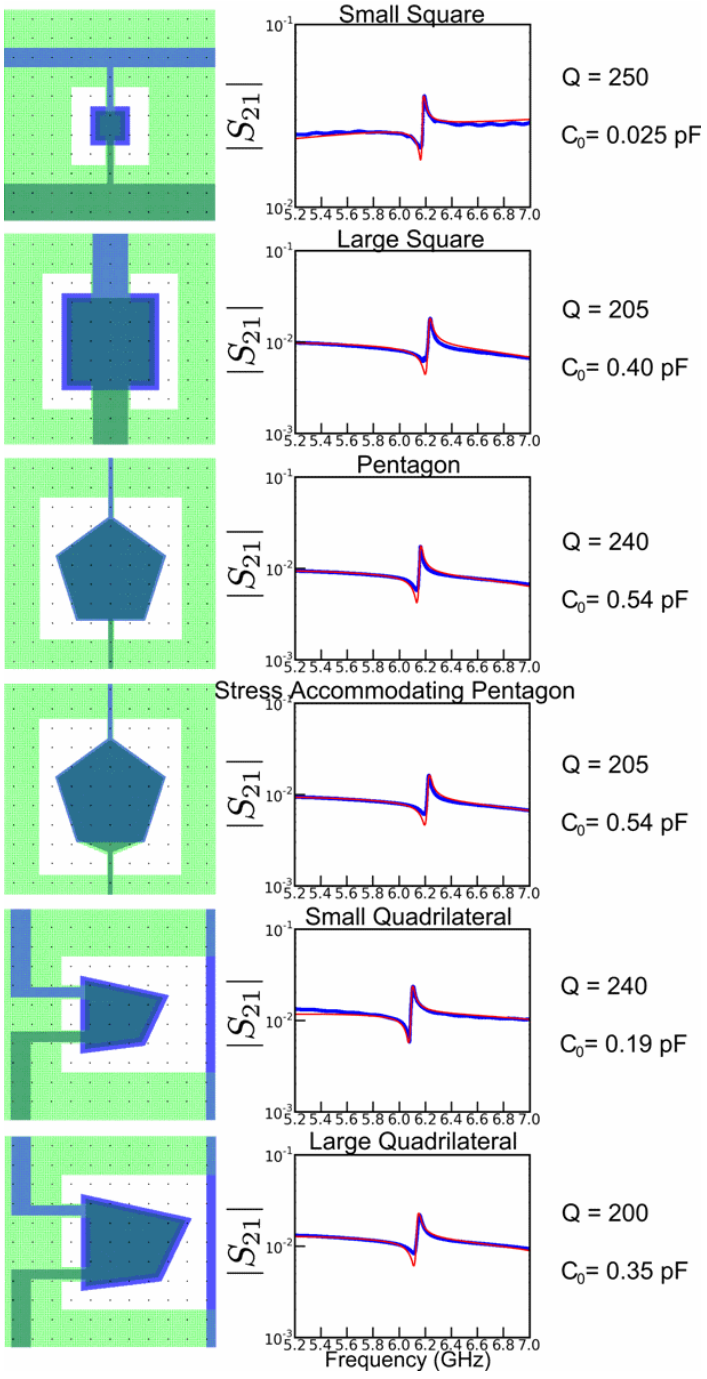

Figure 5.13: Geometry Test – Schematic of various geometries tested, plots of the data measured, fits of the data, the electrical capacitances, and the calculated Qs.

Chapter 6

Conclusions

We successfully fabricated film bulk acoustic resonators. Building a thin film etching device using xenon diflouride, we suspended the FBARs. We were able to measure the FBARs by mounting them in a two-port microwave mount and measure the transmission with a PNA vector network analyzer.

Through our testing and characterization of the FBARs we were able to understand most (but obviously not all) of the features of the measurements. We also found that legwidth and geometry design parameters do not noticeably affect the quality factors of the FBARs.

Using our fabrication process, we created fundamental resonance modes in the FBARs at around 6 GHz with a maximum quality factor of 250. This leads to a calculated energy decay time (T_1) of 6.7 ns, sufficient to couple to a supercon-

ducting phase qubit and transfer quantum states. We are therefore starting the experiment in question.

Chapter 7

Future Work

We can now fabricate the resonators with the appropriate fundamental frequency and energy decay time. We plan to fabricate these film bulk acoustic resonators on-chip with superconducting phase qubits, strongly coupling the two with coupling capacitors. In this way, we plan to transfer the quantum states created with the qubits into the resonators and then measure the states, effectively exploring quantum effects in a classical system.

Bibliography

[1] A.N. Cleland and M.R. Geller. Superconducting qubit storage and entanglement with nanomechanical resonators. *Physical Review Letters*, 93(070501), 2004.

[2] M. Hofheinz et al. Generation of fock states in a superconducting quantum circuit. *Nature*, 454, 2008.

[3] E. Lucero et al. High-fidelity gates in a josephson qubit. *Physical Review Letters*, 100(247001), 2008.